Appl. Phys. B 80, 547–557 (2005)
DOI: 10.1007/s00340-005-1760-2

Applied Physics B
Lasers and Optics

X.P. TANG[1]
A. BECKER[2,✉]
W. LIU[1,2]
S.M. SHARIFI[1]
O.G. KOSAREVA[3]
V.P. KANDIDOV[3]
P. AGOSTINI[1,4,5]
S.L. CHIN[1]

Self-action effects in ionization and fragmentation of toluene by femtosecond laser pulses

[1]Département de Physique, de Génie Physique et d'Optique, Centre d'Optique, Photonique et Laser (COPL), Université Laval, Québec, Québec G1K 7P4, Canada
[2]Max-Planck-Institut für Physik Komplexer Systeme, Nöthnitzer Str. 38, 01187 Dresden, Germany
[3]Department of Physics, International Laser Center, Moscow State University, Moscow 119899, Russia
[4]Comissariat à l'Energie Atomique, DRECAM/SPAM, Centre d'Etudes de Saclay, 91191 Gif-sur-Yvette, France
[5]Max-Born-Institut, Max-Born-Strasse 2a, 12489 Berlin, Germany

Received: 20 August 2004 /
Revised version: 21 December 2004
Published online: 16 February 2005 •

ABSTRACT Occurrence and influence of several self-action effects, induced in the entrance window of a time-of-flight interaction chamber, on the ion and fragment yields of the toluene molecule in the focus of a Ti:sapphire laser pulse are analyzed. Experimental data are obtained using different focusing geometries and are compared with results from numerical simulations using a nonlinear pulse propagation model as well as those from the strong-field *S*-matrix theory. It is shown that (a) self-focusing leads to a displacement of the focus while amplified small perturbations of the input beam result in hot spots in the spatial distribution and in an energy-dependent focus area, (b) small self-phase modulation changes the form of the spectrum and broadens it slightly. A strong increase of the toluene fragmentation appears to correlate to linear and nonlinear changes in the focal spot area, while the scenario of excitation of Raman modes proposed in an earlier publication is ruled out as the dominant effect.

PACS 42.65.Jx; 33.80.Rv; 33.80.Wz

1 Introduction

With the development of ultra-fast intense laser technology and the commercialization of Ti:sapphire lasers, peak power of laser pulses could easily reach GW and even the TW and PW regimes. During the propagation of such an ultra-intense laser pulse inside optical media, nonlinear effects will be induced. This can lead to a strong self-transformation of the laser pulse in space and time, which may finally result in the occurrence of the filamentation phenomenon (e.g. [1–5]). In the application of ultra-fast intense laser pulses to interaction experiments it is difficult to avoid a nonlinear self-transformation of the pulse, since the laser pulse will have to pass through various optical media before reaching the interaction volume. Optical components such as a focusing lens, the entrance window of a vacuum chamber, and even the air path in between are typical elements of an experiment designed to measure ionization and fragmentation yields of atoms and molecules. The influence of these optical components has to be considered, especially when the laser power is high. Even in experiments using a concave mirror inside the vacuum chamber instead of a focusing lens, the entrance window remains a possible source of nonlinear propagation effects. A linkage of the compressor directly to the vacuum system would require a tremendous effort to clean up and pump down the compressor chamber to low pressures of about 10^{-8} Torr, which is not feasible most of the time.

There are several self-action effects which could be foreseen to potentially influence the measurement of ion or fragment yields. Self-focusing of the beam [6–8] can result in a displacement of the whole focal volume in the interaction zone (whole-beam self-focusing) and distortions of the spatial intensity distribution at the focus (small-scale self-focusing). Since multiphoton/tunnel ionization and fragmentation are highly nonlinear processes, they may depend on such intensity variations in the focal region. Self-focusing appears when the laser-beam power exceeds the critical power $P_{\mathrm{crit}} = 3.77\lambda^2/8\pi n_0 n_2$ [6], where λ is the laser wavelength and n_0 and n_2 characterize the intensity-dependent index $n = n_0 + n_2 I$, where I is the laser intensity. For gases around one atmospheric pressure, the critical power is several GW, while for transparent condensed matter the limit is several MW at the Ti:sapphire wavelength. Usually, whole-beam self-focusing occurs first, while small-scale self-focusing sets in at higher laser powers. All lasers commonly used in an intense-field ionization and fragmentation experiment exceed the critical power of the lens or the entrance window significantly.

Further, the spectral content of the laser pulse could be increased up to a supercontinuum spectrum [4, 5, 9] due to self-phase modulation (SPM) [10–12] and self-steepening

✉ Fax: +49-351-871-2299,
E-mail: abecker@mpipks-dresden.mpg.de
All experiments were done at Université Laval, Québec, Canada.

[13, 14]. A consequence of the spectral broadening in an interaction experiment has been indicated by Müller et al. recently [15, 16]. They reported a strong enhancement of fragmentation of the toluene molecule with 80-fs laser pulses, when self-phase modulation was induced by the CaF_2 entrance window of their mass spectrometer. The enhancement was observed for moderate broadening of the spectrum of the pulse. The dissociation was attributed as due to the absorption of the additional frequencies of the supercontinuum spectrum by the Raman-active modes of the neutral molecule or parent ion. Molecules with a high internal vibrational energy are created, which are very likely to dissociate.

Thus, yields of molecular ionization and fragmentation in an intense laser field may be affected significantly by nonlinear pulse propagation effects. It seems to be timely to shed further light on this aspect of interaction experiments, e.g. in view of the recent discrepancies in the results of photofragmentation of large molecules reported by several groups ([15] and references therein). An analysis of the influence of propagation effects can help to establish conditions under which 'pure' results from the interaction with a well-shaped laser pulse around a central wavelength at the focal volume can be obtained. On the other hand, the deformation of a pulse may have its own merit in high-intensity physics, e.g. for time-resolved broadband absorption and excitation spectroscopy or enhancement of molecular fragmentation.

In this paper we investigate the influence of the above-mentioned self-action effects induced by the entrance window of a vacuum chamber on the parent ion and the fragment yields of the toluene molecule in the focus of a Ti:sapphire laser pulse. Results are obtained with different experimental set-ups using two focusing lenses ($f = 500$ mm and $f = 200$ mm) in order to demonstrate the effects of self-transformation of the laser pulse. The whole-beam self-focusing effect results in a displacement of the focal volume, small perturbations in the input beam are amplified to hot spots in the spatial intensity distribution of the pulse at the focus, and self-phase modulation results in a broadening of the spectrum. We illuminate these effects by our experimental observations as well as by results of numerical calculations within a theoretical model of nonlinear pulse propagation considering the passage of the pulse through the different optical elements of the present experimental set-up.

The paper is organized as follows. In Sects. 2 and 3 we briefly describe the different experimental set-ups, followed by a brief sketch of the theoretical models for strong-field ionization and pulse propagation. Next, we demonstrate the displacement of the focal volume at high pulse power. Experimental data obtained with the different set-ups will be compared with each other and with theoretical predictions from Gaussian pulse propagation theory. Then, numerical results will be presented which demonstrate the enhancement of small-amplitude variations in the laser pulse in the entrance window and provide information about the spatial intensity distribution at the focus. These results are compared with pictures of the focal area taken by a CCD camera in the experiment. Finally, we compare the experimental data of the yields of the parent ion with predictions from a strong-field S-matrix theory of ionization of polyatomic molecules and identify the reason for the observed enhancement of the molecule.

2 Experimental set-up

The experiment employs a commercial laser system (built by Spectra Physics at Université Laval) which consists of a Ti:sapphire oscillator (Tsunami) followed by a regenerative and two-pass Ti:sapphire amplifier (Spitfire). The laser pulses have a central wavelength of 800 nm and are operated at a repetition rate of 1 kHz. The compressed pulse has a pulse duration of 39 fs (FWHM) measured by a single-shot auto-correlator (made by Positive Light) and the maximum output energy is 1.8 mJ/pulse.

The laser pulse is focused into the interaction chamber using different focusing lenses. A pyroelectric energy meter (Molectron EPM 1000) is placed behind the last mirror in the laser path to monitor the laser energy by detecting the leak of the mirror. Figure 1a–c show the three set-ups used in the experiment in order to vary the strength of the self-action effects in the entrance window of the vacuum chamber. We have used two lenses with $f = 500$ mm (CaF_2, thickness of 5 mm) and $f = 200$ mm (BK7, thickness of 5 mm), respectively. Further, for the longer focusing lens the distance between the lens and the fused-silica entrance window (thickness of 5 mm) of the vacuum chamber is varied by using an additional pipe of about

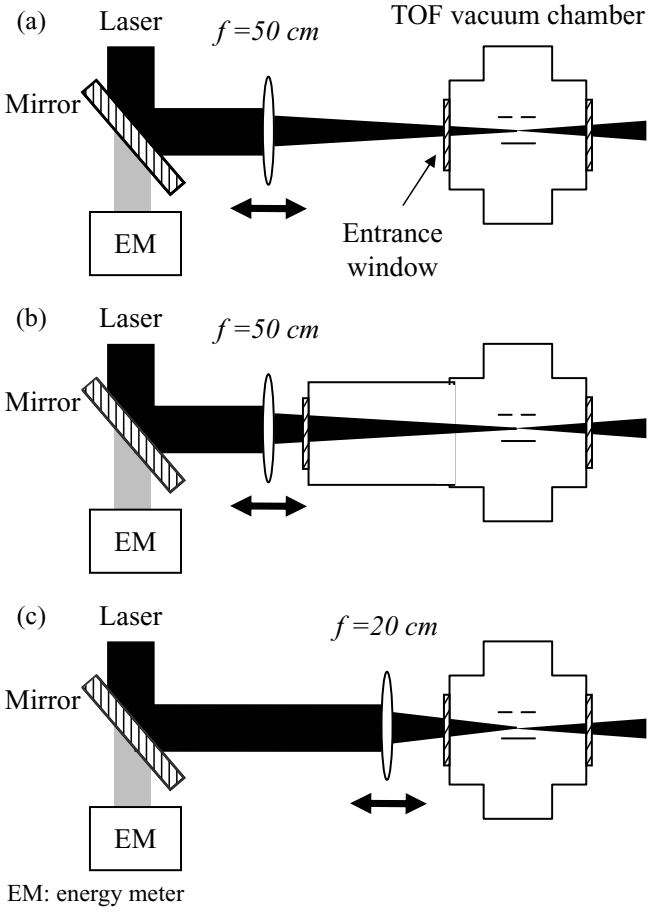

FIGURE 1 Three experimental set-ups for the measurement of the ion yields. The length of the focusing lens and the position of the entrance window with respect to the lens are changed in order to vary the strength of the self-action effects in the window. **a** $f = 500$ mm, large distance between lens and window (strong self-action effects), **b** $f = 500$ mm, short distance between lens and window (small self-action effects), and **c** $f = 200$ mm, short distance between lens and window (small self-action effects)

300-mm length (Fig. 1b). We put the lens holder on a transferring stage and scan the position of the lenses around the optimum position; details will be discussed in Sect. 4.1. The distance between the window and the center of the interaction zone was 15 cm without pipe and 45 cm with pipe. Any nonlinear deformation of the pulse should be the stronger the higher is the laser intensity on the entrance window. Therefore, we expect that self-action effects should occur first for the set-up shown in Fig. 1a, when the laser energy is increased.

Toluene molecules are injected into the high-vacuum chamber of the time-of-flight mass spectrometer through a variable-leak valve. The background pressure was 4×10^{-8} Torr, while the pressure of gaseous toluene molecules was 2×10^{-7} to 5×10^{-4} Torr. The toluene molecules interact with laser pulses and the parent and fragment ions are accelerated by a static field of 500 V/cm towards the ion detector through an opening of 2-cm diameter followed by a field-free flight path of 40 cm. An electron-multiplier tube (EMT, Thorn EMI electron tube, type: 105 EM) with a $\phi = 21.6$-mm detection area was used to detect the ions. The signals at different laser energies were recorded by a 500-MHz oscilloscope (Tektronix TDS 504A).

Measurements of the focal spot area, the averaged laser intensity, and the pulse spectrum have been carried out outside the chamber, as shown in Fig. 2. The lens and the window are kept in the same relative positions as in the different set-ups for the interaction experiment but the beam is reflected by a wedge ($\lambda/10$ surface quality) set immediately after the window to reduce the power to the point where self-focusing in air is avoided. For the focal spot measurement the focus is imaged by a lens ($f = 10$ cm) onto a CCD camera (Cohu 4810) with a magnification of 18 (cf. Fig. 2a). The CCD camera pictures are captured by a computer. The laser intensity at the focus was calculated from the laser pulse energy, the pulse duration, and the measured focal area as $I_{\mathrm{avg}} = W/(\pi ab\tau_{\mathrm{FWHM}})$, where W is the pulse energy and a and b are the half-axes of the beam cross section along the rectangular coordinates defined at $1/e^2$ fluence level of the experimentally measured focal spot size. I_{avg} is considered as the averaged intensity at the focal spot in the vacuum chamber; it equals one-half of the *peak* intensity I_0 under the assumption of a symmetric ($a = b$) Gaussian spatial intensity distribution at the focal spot. The pulse spectrum was recorded by a spectrometer (SpectroPro 150 by ARC, cf. Fig. 2b).

3 Theory

The experimental data are analyzed by comparison with the results from a pulse-propagation model and the first-order term of a strong-field S-matrix theory for ionization of molecules. Both models have been introduced and applied successfully before. Therefore, we restrict ourselves here to a brief sketch of the approaches and refer the reader to the earlier references for the details.

3.1 *Pulse-propagation model*

Traditionally, the transformation of the pulse in the course of optical-field-induced ionization experiments is

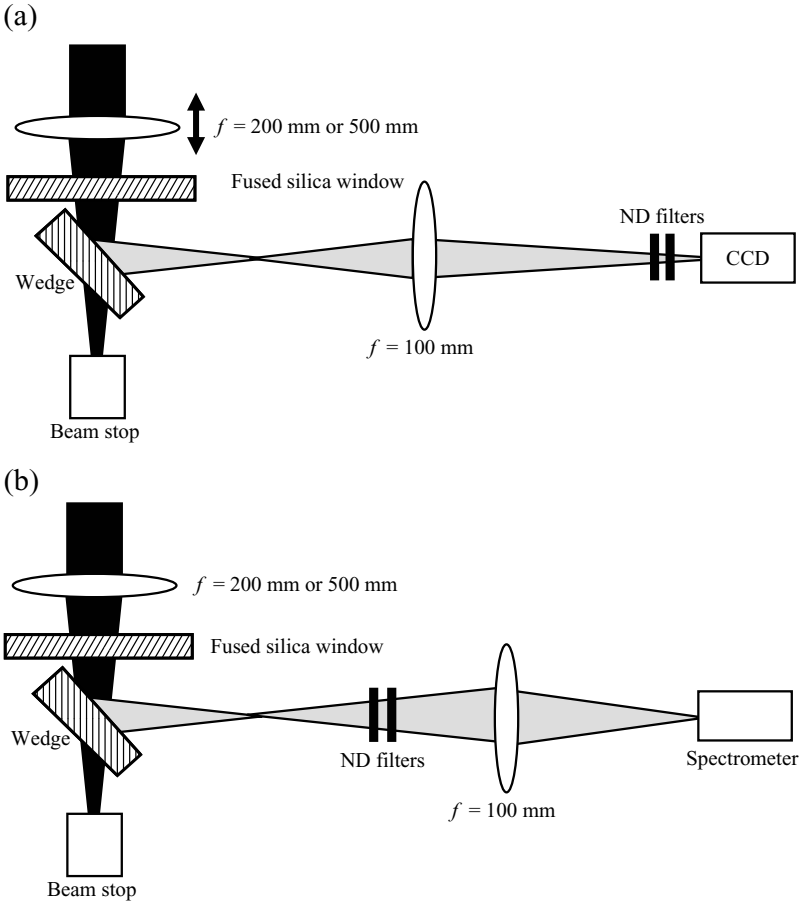

FIGURE 2 **a** Set-up for the measurement of the focal area outside the vacuum chamber. The beam is focused through lenses of different focusing lengths and passes through a CaF_2 window; the position of both elements are kept the same as in the interaction experiment. A wedge is used to reduce the beam power immediately after the window to avoid additional self-focusing effects in air. The focal area is imaged onto a CCD camera using another lens and neutral-density filters. **b** Set-up for the measurement of the pulse spectrum at the focus outside the vacuum chamber

described in terms of linear propagation [17]. At the entrance to the medium the spatial pulse distribution is typically considered as a TEM_{00} Gaussian with Gaussian temporal profile. In this case the overall spatio-temporal distribution of the radiation in the geometrical focus located inside the interaction chamber is given as a product of the spatial profile in the focus, calculated according to the linear diffraction theory, and the initial Gaussian temporal profile. The intensity distribution $I(x, y, z = f; t)$ is then used for the calculation of the ion yield from the rate equations. Here $z = f$ is the position of the geometrical focus.

In the present experiment, the propagation of the pulse cannot be considered in terms of linear diffraction, since self-focusing in the optical elements, especially in the input window of the interaction chamber, cannot be neglected. Indeed, the maximum nonlinear phase growth φ_{nl} inside the fused-silica window attained on the beam axis in the plane-wave approximation is as large as [18]

$$\varphi_{\mathrm{nl}} = \frac{1}{2n_0} k n_2 |E|^2 \Delta z \approx 1.6\pi \tag{1}$$

for a 700-μJ pulse with the duration 39 fs (FWHM) focused with a 500-mm lens into the interaction chamber with the input window located at a distance of 15 cm before the geometrical focus. The value given by Eq. (1) is the equivalent of the usual B-integral defined in [8]. The peak pulse intensity at the chamber window is $I = (c/8\pi)|E|^2 = 10^{12}\,\mathrm{W/cm^2}$ and the propagation distance $\Delta z = 5\,\mathrm{mm}$ is equal to the width of the window in the present experiment. The wave number $k = 2\pi/\lambda$ corresponds to the laser central wavelength of 800 nm and $n_2 = 3.7 \times 10^{-16}\,\mathrm{cm^2/W}$ for fused silica [19]. The phase growth $\varphi_{\mathrm{nl}} \approx 1.6\pi$ is large enough to provide noticeable self-action in the window. The nonlinear phase growth in air is approximately 0.01π radians ($n_2 \approx 10^{-19}\,\mathrm{cm^2/W}$ [19]) and in the focusing lens 0.07π radians (CaF_2, $n_2 \approx 10^{-16}\,\mathrm{cm^2/W}$ [19]). Therefore, the entrance window of the vacuum chamber can be considered as the main source of distortions in the pulse transformation in the present experimental set-ups.

We have performed numerical simulations to study the temporal and spatial intensity distribution of the pulse at the focus inside the interaction chamber. Assuming that pulse propagation occurs along the z axis with the group velocity v_{g}, the equation for the slowly varying amplitude of the light field $E(x, y, z; t)$ is given by

$$2\mathrm{i}k\left(\frac{\partial E}{\partial z} + \frac{1}{v_{\mathrm{g}}}\frac{\partial E}{\partial t}\right) = \frac{\partial^2 E}{\partial x^2} + \frac{\partial^2 E}{\partial y^2} + \frac{2k^2}{n_0}\Delta n, \tag{2}$$

where the first two terms on the right-hand side of Eq. (2) describe diffraction. In the third term we successively take into account the Kerr nonlinearity of the lens, the window, and the air depending on the propagation distance z:

$$\Delta n = \frac{1}{2} n_2 |E|^2. \tag{3}$$

In accordance with the values of the coefficient n_2, the critical power for self-focusing in air is $P_{\mathrm{cr,air}} = 6\,\mathrm{GW}$, in CaF_2 crystal $P_{\mathrm{cr,CaF_2}} = 7.4\,\mathrm{MW}$, and in fused silica $P_{\mathrm{cr,fused\,silica}} = 2\,\mathrm{MW}$.

In Eq. (2) we do not take into account plasma generation and material dispersion in air and in the entrance window of the chamber. Indeed, the peak pulse intensity needed to produce an electron density that is sufficient to affect the pulse propagation is of the order of $2 \times 10^{13}\,\mathrm{W/cm^2}$. Simulations show that the maximum intensity achieved at the output of the window is about $5 \times 10^{12}\,\mathrm{W/cm^2}$ in the geometry shown in Fig. 1a, corresponding to the case of the largest self-action effects. This intensity is well below the ionization-threshold intensity. The group-velocity dispersion in the medium is also neglected in Eq. (2). This can be justified by the fact that for a 39-fs pulse the characteristic length of pulse dispersive broadening in air is about 40 m, while in the fused-silica window this length is of the order of 2 cm. Both distances are much larger than the propagation distance attained in the current experimental set-up. Thus, we can neglect material dispersion in the simulations.

We start the propagation at the position of the focusing lens with the following spatio-temporal distribution of the light field:

$$E(x, y, z = 0, \tau) = E_0 \sqrt{\frac{J(x, y)}{J_{\max}}} \times \exp\left(\frac{-t^2}{2\tau_0^2} + \frac{\mathrm{i}k(x^2 + y^2)}{2f^2}\right), \tag{4}$$

where $I_0 = (c/8\pi)|E_0|^2$ is the peak pulse intensity changing from $6.3 \times 10^9\,\mathrm{W/cm^2}$ for a 50-μJ input pulse energy to $1.125 \times 10^{11}\,\mathrm{W/cm^2}$ for a 900-μJ input pulse energy, $J(x, y)$ is the fluence distribution as measured in the experiment and normalized to its maximum value $J_{\max}$, $\tau_0 = 25\,\mathrm{fs}$ corresponds to a FWHM pulse duration of 39 fs, and f is the geometrical focusing distance equal to either 500 or 200 mm.

3.2 *Strong-field S-matrix theory: ionization rates and yields*

Rates and yields of single ionization of the toluene molecule are calculated using the first-order term of the S-matrix series of strong-field ionization of polyatomic molecules [20, 21]. According to this model, the total rate of ionization of a molecule with N_{e} electrons in its highest occupied molecular orbital in a linearly polarized laser field is given by

$$\Gamma^+(I) = 2\pi N_{\mathrm{e}} \left[\frac{(2I_{\mathrm{p}})^{3/2}}{E_0}\right]^{2/\sqrt{2I_{\mathrm{p}}}} \sum_{N=N_0}^{\infty} k_N (U_{\mathrm{p}} - N\omega)^2 \times \int \mathrm{d}\hat{k}_N J_N^2\left(\vec{\alpha}_{\mathrm{o}} \cdot \vec{k}_N; \frac{U_{\mathrm{p}}}{2\omega}\right) |\langle \phi_{\vec{k}_N} \phi_{\mathrm{f}}^+ | \phi_{\mathrm{i}} \rangle|^2,$$

where $I_{\mathrm{p}} = 8.83\,\mathrm{eV}$ is the ionization energy of the toluene molecule, $J_N(a; b)$ is the generalized Bessel function of two arguments, $\alpha_0 = \sqrt{I}/\omega$ is the quiver radius, $U_{\mathrm{p}} = I/4\omega^2$ is the quiver energy of an electron in the field of frequency ω and peak intensity $I = |E_0|^2$, $k_N^2/2 = N\omega - U_{\mathrm{p}} - I_{\mathrm{p}}$ is the kinetic energy of the electron, and N_0 is the minimum number of photons needed to be absorbed from the field to ionize the molecule. The calculated rates are orientation averaged assuming random orientation of the molecular axes with respect to the laser polarization orientation. The initial

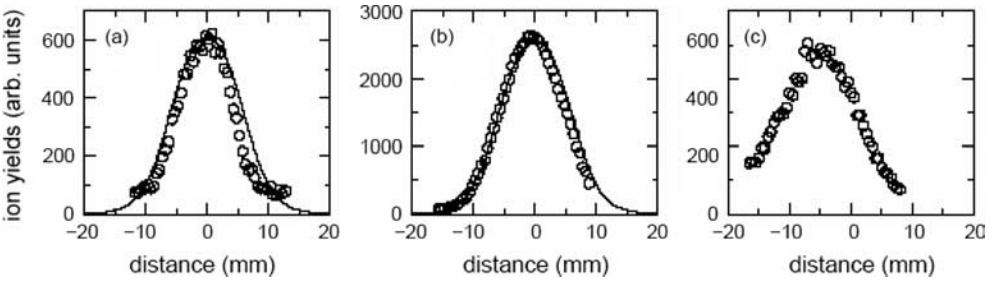

FIGURE 3 Yields of the parent ion (*circles*, **a** and **b**) and for the $C_2H_n^+$ fragment group (*circles*, **c**) as a function of the position of different pulse energies and the experimental set-up, shown in Fig. 1a: **a** 14.5 μJ, **b** 72 μJ, and **c** 590 μJ. Also shown are the predictions of the *S*-matrix theory. The origin of the *x* axis has been set such that the maximum of the distribution at the lowest energies near the detection limit is centered around 0 mm. Negative (positive) values indicate a shift towards (away from) the window

ground-state wave function of the neutral molecule, Φ_i, and the final ground-state wave function of the molecular ion, Φ_f^+, were obtained using the GAMESS code [22].

Experimental data are obtained as ionization yields in the laser focus interaction volume. These yields are determined by combining the fundamental rates with the rate equations giving the populations at any point of the laser focus and integrating over the contributions in the focus. The normalized populations of the neutral molecule and the parent ion at point $(\vec{r}, t)$, $P_0(\vec{r}, t)$ and $P(\vec{r}, t)$, are governed by the rates as

$$\frac{\mathrm{d}P_0(\vec{r}, t)}{\mathrm{d}t} = -\Gamma^+(I(\vec{r}, t))P_0(\vec{r}, t),$$
$$\frac{\mathrm{d}P(\vec{r}, t)}{\mathrm{d}t} = \Gamma^+(I(\vec{r}, t))P_0(\vec{r}, t).$$

The system is solved with the initial conditions $P_0(\vec{r}, t = -\infty) = 1$ and $P(\vec{r}, t = -\infty) = 0$, and integrated over the contributions in the focus. Any temporal and spatial intensity distribution can be used in the calculations, as long as the adiabatic rate condition is fulfilled. In the case of ionization the onset of adiabaticity has been found to occur for pulse durations as short as about three cycles of the field [23].

4 Results and discussion

4.1 *Whole-beam self-focusing: displacement of the focal volume*

Molecular ionization and fragmentation are highly nonlinear processes and depend strongly on the laser intensity. The mass peaks of the parent ion or the ionic fragments in the time-of-flight spectrometer can therefore serve as indicators for the alignment of the highest-intensity region in the vacuum chamber with respect to the opening of the detector. Optimal alignment is achieved by varying the position of the focusing lens until the mass peaks are maximized. In traditional interaction experiments, this position is determined once and then kept constant during the measurement over a range of input laser energies.

We expect that the effect of self-focusing in the entrance window of the vacuum chamber, if any, will lead primarily to a shift of the focal volume towards the window with increase of the laser energy. Thus, we have optimized the position of the lens at all input energies by maximizing the mass peak of an unsaturated ion peak; at low energies the parent ion and above the saturation of single ionization the peak of an ionic fragment group.

In Fig. 3 we present for the set-up with the long focal lens and without pipe (cf. Fig. 1a) the results of our measurements (circles) at three different laser pulse energies, (a) 14.5 μJ, (b) 72 μJ, and (c) 590 μJ. The heights of the parent-ion mass peak (Fig. 3a and b) at the lower energies and those of the $C_2H_n^+(n = 0, 1, 2$, where '0' means the absence of H) fragment group (Fig. 3c) at the highest energy are shown as a function of the position x of the lens. The x axis has been scaled such that the maximum of the distributions at the lowest energies near the detection limit is centered around 0 mm. Negative (positive) values indicate a shift towards (away from) the window.

The experimental data for the parent-ion peaks (panels a and b) are compared with the predictions of the *S*-matrix theory (lines). The latter have been obtained assuming an intensity distribution having a Gaussian shape in time with a FWHM pulse width of $\tau = 39$ fs and a spatial TEM_{00} form with a Rayleigh length of 8.5 mm, as in the experiment. Along the propagation direction the effective interaction zone is restricted in the experiment by the size of the detector opening; in the calculations we have obtained best agreement with the experimental distributions for a size of 1.2 cm, which is slightly smaller than that of the time-of-flight detector in the experiment (2 cm).

It can be seen from Fig. 3 that the optimal position of the lens is determined in the present experiment within about ± 1 mm. As expected, a shift of the optimal position towards the window is seen at the higher laser energies, of about 1 mm at 72 μJ (Fig. 3b) and about 5 mm at 590 μJ (Fig. 3c). Please note also that at the highest input laser energy the distribution is asymmetrical, which is an indication of a distortion of the spatial focal volume distribution (cf. Sect. 4.2).

The shift of the focus with respect to the geometrical focus as a function of the input energy is shown in Fig. 4a for the 500-mm lens without pipe (solid squares) and with pipe (open circles) and in Fig. 4b for the 200-mm lens. The strong displacement of the focus, up to about 5 mm at the highest energies, for the set-up with the long focal length without pipe clearly demonstrates the effect of whole-beam self-focusing. For the other two set-ups the optimal position of the lens remains almost unchanged (within the experimental error of ± 1 mm). This is in agreement with our expectation that any self-action effects should be strongest for the set-up in Fig. 1a.

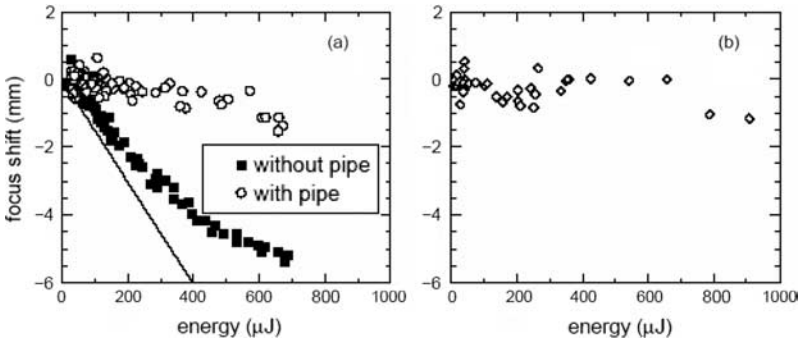

FIGURE 4 Optimum position of the focusing lens for alignment of the focal area with respect to the opening of the detector. A shift of the lens of distance D toward the entrance window compensates the displacement of the focus due to self-focusing of the whole beam. **a** $f = 500$ mm, *solid squares* (experimental data obtained without pipe, Fig. 1a), *open circles* (experimental data obtained with pipe, Fig. 1b), *line* (theoretical estimation, see text), **b** $f = 200$ mm (Fig. 1c)

A simple estimate of the focusing distance F of the pulse resulting from both geometrical focusing and self-focusing effects, introduced by the various optical elements, is given by

$$\frac{1}{F} = \beta_{\text{lens}} + \beta_{\text{air}} + \beta_{\text{window}} + \beta_{\text{geometrical}}, \tag{5}$$

where β_{lens}, β_{air}, and β_{window} are the wavefront curvatures introduced by the focusing lens (treated as a piece of the nonlinear medium), the air and the entrance window of the chamber. For a Gaussian beam shape the curvature is determined by [18]:

$$\beta = \frac{\Delta z/\left(ka_0^2\right)^2}{(1 - P/\text{cr})^{-1} + \Delta z^2/\left(ka_0^2\right)^2}, \tag{6}$$

where Δz is the width of the corresponding nonlinear medium, a_0 is the radius of the Gaussian beam at e^{-1} intensity level, and P_{cr} is the critical power for self-focusing in this medium. The curvature $\beta_{\text{geometrical}} = 1/f$ is introduced into the beam due to the geometrical focusing. For the case of 700-μJ input pulse energy and geometrical focusing with a 500-mm lens without pipe the relative contribution of the nonlinear curvature $\beta_{\text{lens}} + \beta_{\text{air}} + \beta_{\text{window}}$ to the total curvature $1/F$ is 0.51%, while for the case of the 200-mm lens this contribution decreases approximately three times to 0.18%. This value demonstrates the effect of stronger geometrical focusing in the case of a shorter focal length and, hence, the smaller focal spot shift $f - F$. This rough estimate of the focal spot shift is shown for the 500-mm lens without pipe by the line in Fig. 4a. The agreement at lower energies is good; the deviation at higher energies is again due to the variation of the spatial intensity distribution, to be discussed below.

4.2 *Small-scale self-focusing: intensity variations in the focal volume*

Besides the tendency of the beam to self-focus as a whole, it is known (e.g. [7, 8]) that on a small scale natural perturbations in the beam profile can be enhanced via self-focusing. For the propagation of a beam in a nonlinear medium this can finally result in the break-up of the beam and multiple filamentation [24]. In order to investigate the effect of small-scale self-focusing in the fused-silica entrance window on the intensity distribution at the focus, we have performed numerical calculations using the propagation model discussed above and measurements of the focal spot area using the set-up shown in Fig. 2a.

In the simulations we have used the transverse fluence distribution $J(x, y)$ measured in the experiment, an input pulse duration of 39 fs, and different pulse energies as initial condition. The propagation of the pulse through the lens and the air towards the entrance window and finally in the vacuum chamber has been simulated until the minimum radius of the pulse is reached. Specifications of the optical elements, such as thicknesses and materials, as well as distances between the optics have been chosen to be the same as in the experimental set-up. As discussed above, self-focusing effects are stronger the longer is the focal length of the lens. We have therefore performed simulations for the $f = 500$-mm lens without pipe.

In Fig. 5 we present the simulated spatial intensity profile of the beam with input energy of 750 μJ. Distributions at specific points are shown as a function of the transverse beam extension, namely (a) at the entrance window, (b) just after the entrance window, and (c) at the focus. The intensities are scaled to the peak intensity at the entrance window. Please note the 400-times increase in the maximum intensity and the nine-time decrease in the extension of the transverse spatial region in Fig. 5c compared to the other panels.

The comparison in Fig. 5 illuminates the effects of the different optical elements on the pulse profile. As can be seen from Fig. 5a the transverse input intensity distribution is not symmetrical with a shoulder on one side and has further natural perturbations over the whole profile. During the propagation of the pulse through the lens and the air towards the entrance window this profile remains almost unchanged, except for the decrease in its transverse extension due to the external focusing. After the entrance window the main profile of the beam with the shoulder is still visible, but the natural small-scale perturbations of the beam profile are strongly enhanced and hot spots are developed (Fig. 5b). Finally, at the focus one observes a central main peak with side wings (Fig. 5c).

The wings are formed from the enhancement of the *small perturbations* in the input beam profile to hot spots in the entrance window, which afterwards undergo linear diffraction in the vacuum chamber. We may stress that they are not due to the nonsymmetric main profile of the input pulse. While it might always be feasible to improve the main profile of a laser output, small perturbations usually cannot be avoided. Consequently, the development of hot spots or wings at the focus due to small-scale self-focusing in the entrance window may occur for any input pulse at high energies.

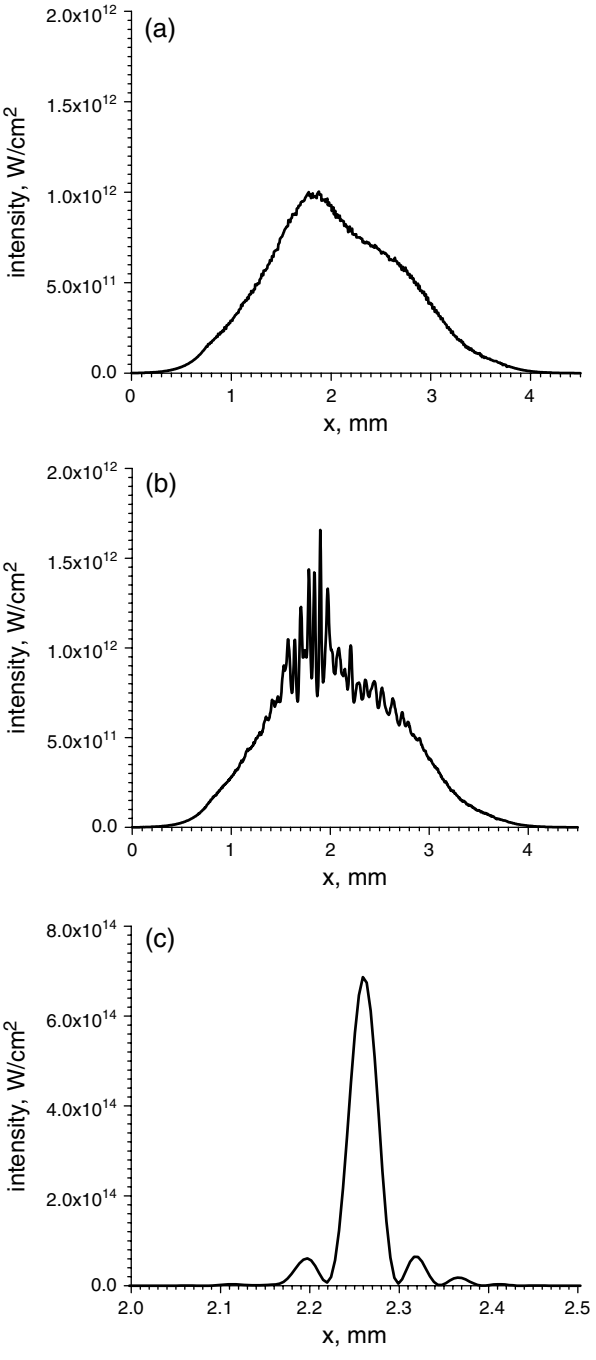

FIGURE 5 Results of numerical calculations for the transverse intensity distribution at different propagation distances using a pulse-propagation model. **a** At the entrance window, **b** just behind the entrance window, and **c** at the focus. The input transverse beam profile has been measured in the experiment and the pulse energy was 750 μJ. Other laser parameters were 39 fs and 800 nm. A focusing lens with $f = 500$ mm (without pipe) has been considered in the simulations

Small-scale self-focusing leads also to an increase of the focal spot area. This might be understood as follows: the initial single mode of the laser is changed due to the nonlinear effects in the window into higher-order multimodes as the pulse energy increases. Since higher-order modes cannot be focused well, the spot size increases. This is seen from the comparison of the transverse fluence distributions in the focal spot of the $f = 500$-mm lens at different input pulse energies, shown in Fig. 6. Experimental data (panels a–c in the upper row) and numerical results from the pulse-propagation model (panels d–f in the lower row) are presented as equal-intensity contours. Each transverse distribution is normalized to its maximum value and the lowest equal-intensity contour corresponds to 0.03 of the maximum value. The interval between the contours is changing as 2^n, where n is the contour number. Since changes in the intensity distribution in the time domain are small in the course of propagation through optical elements, the transverse fluence distribution in the simulations is similar to the transverse intensity distribution in the center of the pulse. Thus, in panels d–f of Fig. 6 one can see the intensity distribution in the center of the pulse. The spatial coordinates x and y are normalized to the beam radius a_{50} obtained at $1/e^2$ level of intensity at a low energy of 50 μJ.

A consequence of the increase of the focal spot area should be that the laser intensity (peak intensity as well as averaged intensity, see definition in Sect. 2) does not grow linearly with the pulse energy, but starts to saturate at high energies. This is seen from Fig. 6, where in panels d–f the peak intensity saturates with increasing input pulse energy. In panel d the simulated peak intensity is 0.85×10^{14} W/cm^2 for 50 μJ, in panel e it is 5.6×10^{14} W/cm^2 for 400 μJ, and in panel f it is 6.8×10^{14} W/cm^2 for 600 μJ. The same effect is also apparent in Fig. 7, where the measured averaged laser intensity is shown as a function of the input pulse energy. Curves are plotted for the different set-ups ($f = 500$ mm, without pipe: solid squares, $f = 500$ mm, with pipe: open circles). For $f = 500$ mm (without pipe) the expected deviation from the linear dependence is seen above 300 μJ (or averaged intensities above 10^{14} W/cm^2, respectively). For the other two set-ups the averaged intensity is found to remain proportional to the input pulse energy over the whole energy range used in the experiments.

4.3 *Parent-ion yields*

As shown above, both the self-focusing effects, of the whole beam and on small scales inside the beam profile, can lead to changes in the spatial intensity distributions of the focal volume. In an analysis of multiphoton/tunnel ionization (and fragmentation) of atoms and molecules these effects should be taken into account. It can be partially done in the experiment: the displacement of the focal volume with respect to the detector opening can be corrected by optimizing the position of the focusing lens, as described in Sect. 4.1. A deviation from the linear dependence of the averaged (and peak) intensity on the input pulse energy due to an increase of the focal spot area can be taken into account by measuring a calibration curve, as presented in Fig. 7. On the other hand, it seems to us that variations of the spatial intensity distribution from the usually assumed Gaussian shape might be best considered in the theoretical analysis of the experimental data.

In Fig. 8 we present a comparison between the experimental data (solid squares) and the predictions of the S-matrix theory (lines) for the yields of the parent ions $C_7H_8^+$ as a function of the averaged laser intensity. The experimental data are obtained using (a) the $f = 500$-mm lens, without pipe and (b) the $f = 200$-mm lens. The position of the lenses has

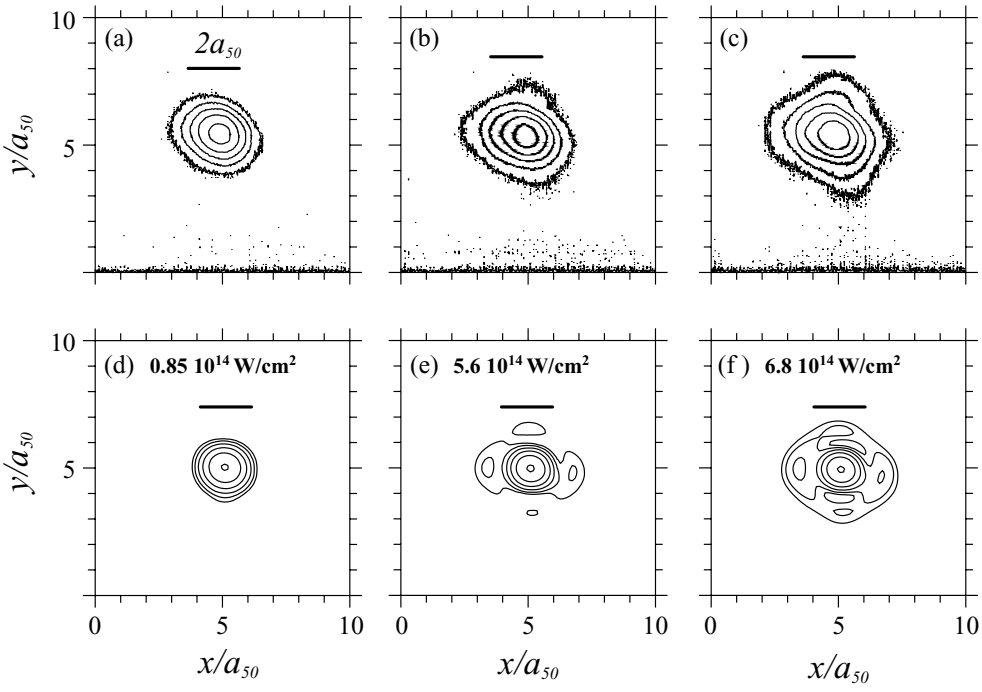

FIGURE 6 Comparison of experimental data (**a–c** in the *upper row*) and results of numerical calculations (**d–f** in the *lower row*) of the fluence distribution in the focal area using a $f = 500$-mm lens (without pipe) at different pulse energies, **a** 50 μJ, **b** 400 μJ, and **c** 600 μJ. Other laser parameters were as in Fig. 5. The lowest contour value is 0.03 of the maximum contour value in all distributions. The interval between the contours changes as 2^n, where n is the contour number. The horizontal scale indicates the diameter $2a_{50}$ of the fluence distribution obtained at 50 μJ at $1/e^2$ level. The peak intensity, as obtained in the simulations, is indicated in (**d–f**) (in W/cm^2)

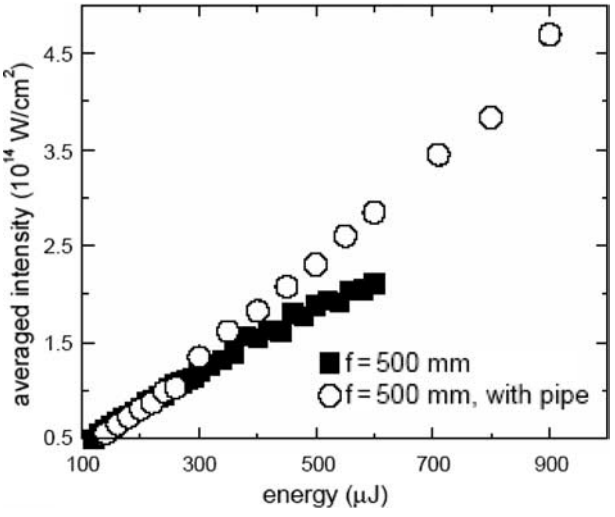

FIGURE 7 Results of the measurements of the averaged laser intensity at the focus as a function of the input pulse energy obtained for the different set-ups: $f = 500$ mm, with pipe (*open circles*), $f = 500$ mm, without pipe (*solid squares*)

been optimized for all energies and the intensity-to-energy calibration curves have been used. The theoretical results are calculated assuming a Gaussian spatial and temporal intensity distribution at the focus. Since the experimental signals are not obtained on an absolute scale, the theoretical results are matched to the experimental data at one point; the intensity axis is unchanged.

The theoretical predictions agree very well with the experimental data. The agreement for both the experimental set-ups shows that the correction of the self-focusing effects, made in the case of the $f = 500$-mm lens, has been successful. The slight deviations from the Gaussian distribution at the largest intensities (cf. Fig. 6) obviously do not affect the results, since they are not taken into account in the theoretical analyses.

4.4 *Fragmentation yields*

While self-focusing of the pulse leads to distortions of the pulse in its spatial shape, self-phase modulation can change the pulse form in time. As outlined in the introduction, it has been observed [16] that a moderate broadening of the pulse spectrum due to self-phase modulation leads to a strong enhancement of fragmentation of the toluene molecule. In order to shed further light on this self-action effect, we have measured the yields of the fragment ions for the three set-ups.

The mass spectra of toluene at three averaged laser intensities, observed using the $f = 500$-mm lens without pipe (panel a), the $f = 500$-mm lens with pipe (panel b), and the $f = 200$-mm lens (panel c) are shown in Fig. 9. Please note that the mass spectra in the same row are recorded at (almost) the same averaged laser intensity. For the sake of comparison, all spectra are scaled such that the mass peak of the parent ion is equal to 1000. It is seen from the comparison that fragmentation is much stronger for the $f = 500$-mm lens than for the $f = 200$-mm lens. Most interestingly, however, the amount of fragmentation does not change significantly whether the pipe is used in the case of the longer focal lens or not. This indicates that the main origin for the enhanced fragmentation rate for the longer lens cannot be due to a nonlinear effect, but has to result from the change of the focusing geometry.

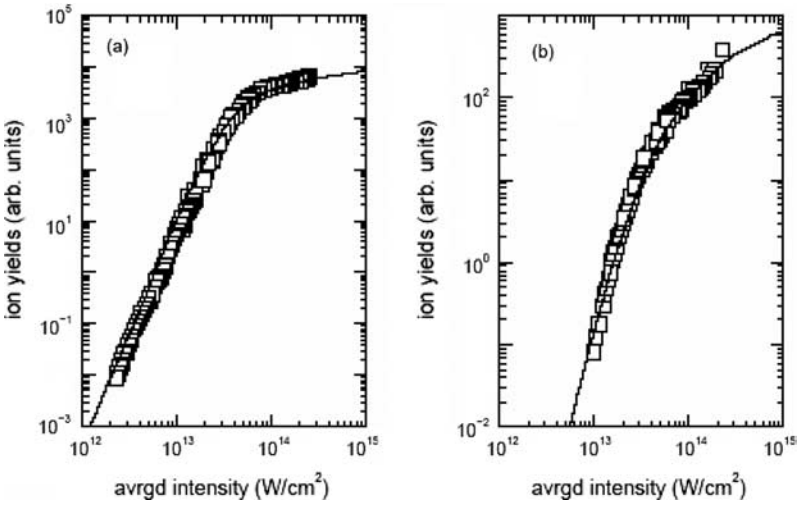

FIGURE 8 Yields of the parent toluene ion as a function of the averaged laser intensity. A comparison is shown between the experimental data (*solid squares*) and results of the *S*-matrix theory (*lines*). The experimental yields are obtained with the 500-mm lens (**a**) and the 200-mm lens (**b**), respectively. Laser wavelength: 800 nm, pulse duration: 39 fs

In order to investigate this effect, we have performed numerical calculations of the ratio of the yield of one fragment (CH^+) to the yield of the parent ion. The fragmentation channel leading to this fragment is unknown; in our model we have therefore made the following assumptions. The parent ion and fragment yields are determined via an extension of the rate equations in Sect. 3.2 as

$$\frac{\mathrm{d}P_0(\vec{r},t)}{\mathrm{d}t} = -\Gamma^+(I(\vec{r},t))P_0(\vec{r},t),$$

$$\frac{\mathrm{d}P(\vec{r},t)}{\mathrm{d}t} = \Gamma^+(I(\vec{r},t))P_0(\vec{r},t) - \Gamma_{\mathrm{frag}}(I(\vec{r},t))P(\vec{r},t),$$

$$\frac{\mathrm{d}P_{\mathrm{CH}^+}(\vec{r},t)}{\mathrm{d}t} = \Gamma_{\mathrm{CH}^+}(I(\vec{r},t))P(\vec{r},t).$$

Thus, we assume that the fragment is created from the parent ion. The rate of fragmentation, Γ_{CH^+}, is determined empirically, such that the numerical result for the ratio P_{CH^+}/P equals the experimental value for the $f = 200$-mm lens, assuming an undisturbed Gaussian intensity distribution and a detector opening of 1.2 cm. Using this empirical fragmentation rate we have performed calculations for the $f = 500$-mm lens using an undisturbed Gaussian distribution (experimental set-up with pipe) and the simulated nonlinear distribution (Fig. 6f, experimental set-up without pipe).

The results of our calculations for the ratio P_{CH^+}/P for the input energies in the lower row in Fig. 9 are compared with the experimental data in Table 1. As in the experimental data, we observe a clear enhancement of the fragment yield in the case of the 500-mm lens, in good agreement with the experimental observations. We conclude that the enhancement of the fragment yields (relative to the parent-ion yield) in our experimental set-up is due to linear and nonlinear changes in the intensity distribution in the effective interaction zone (seen by the detector). Above saturation (i.e. above $\approx 7 \times 10^{13}$ W/cm^2) parent ions are created at lower-intensity regions in the outer parts of the intensity distribution, while the fragments are created in its center. As the focal length becomes longer the larger the focal spot area becomes and, hence, low-intensity regions quickly move outside the effective interaction zone when the pulse energy is increased. As a result, the observed fragmentation rate seems to increase. This effect is further enhanced when there is an additional nonlinear increase of the focal spot area. This focal spot increase is the result of the diffraction of the distorted spatial profile at the output of the chamber window. The profile is distorted by the hot spots formed in the window in the set-up with the 500-mm lens without pipe (cf. Fig. 6).

Focal distance	Experiment	Simulations
$f = 200$ mm	0.06	0.06
$f = 500$ mm, with pipe (Gaussian distribution)	0.26	0.19
$f = 500$ mm, without pipe (distorted distribution)	0.30	0.32

The input energies as in Fig. 9, lower row. Average intensity is $\approx 2 \times 10^{14}$ W/cm^2 for all cases shown in the table

TABLE 1 Comparison of experimental data and numerical simulation results for P_{CH^+}/P

We have also investigated whether there is also a relation of the enhancement of fragmentation with a self-phase modulation in the entrance window. To this end, we have measured the pulse spectra at the focus using the set-up in Fig. 2b. In Figs. 10a and 11a comparisons of the spectra at low (solid lines) and high input energies (dashed lines) for the two set-ups are shown. While for the $f = 200$-mm lens (Fig. 11) the width of the spectrum remains almost unchanged with increase of the pulse energy, in the case of the $f = 500$-mm lens (Fig. 10) the shape of the spectrum changes and becomes slightly broadened in its wings. In panels b of Figs. 10 and 11 we have plotted the width of the spectra at different levels (FWHM: squares, $1/e^2$: circles, and 3%: triangles). For the $f = 500$-mm lens (Fig. 10b), the widths at both the higher levels first decrease; when the energy increases, they show a minimum at about 300–400 μJ before they increase again. In the wings of the spectrum (3% level) the width increases from about 200 μJ onward. On the other hand, for the $f = 200$-mm lens the widths remain constant at all levels over the whole energy range.

Our observations agree to a certain extent with those of the previous experiment [16], since we do observe a correlation between changes in the spectrum and an enhancement of the fragmentation of the toluene molecule. However, the changes in the shape of the spectrum and the broadening are much

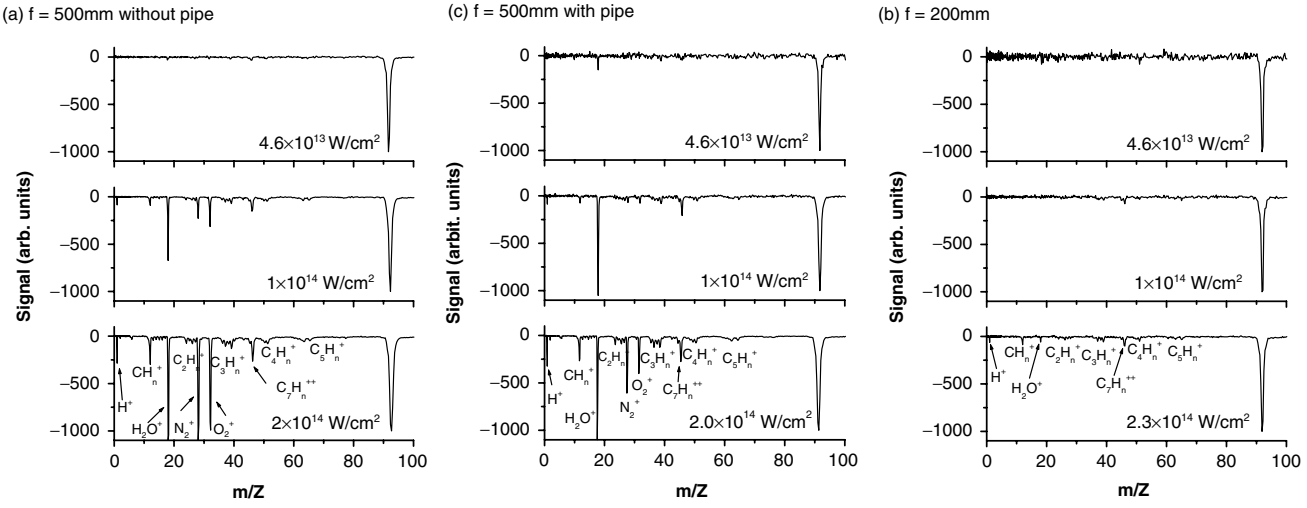

FIGURE 9 Mass spectra of toluene molecule obtained **a** with $f = 500$-mm lens, without pipe, **b** with $f = 500$-mm lens, with pipe, and **c** with $f = 200$-mm lens. Spectra in the same row are recorded at (almost) the same averaged intensity

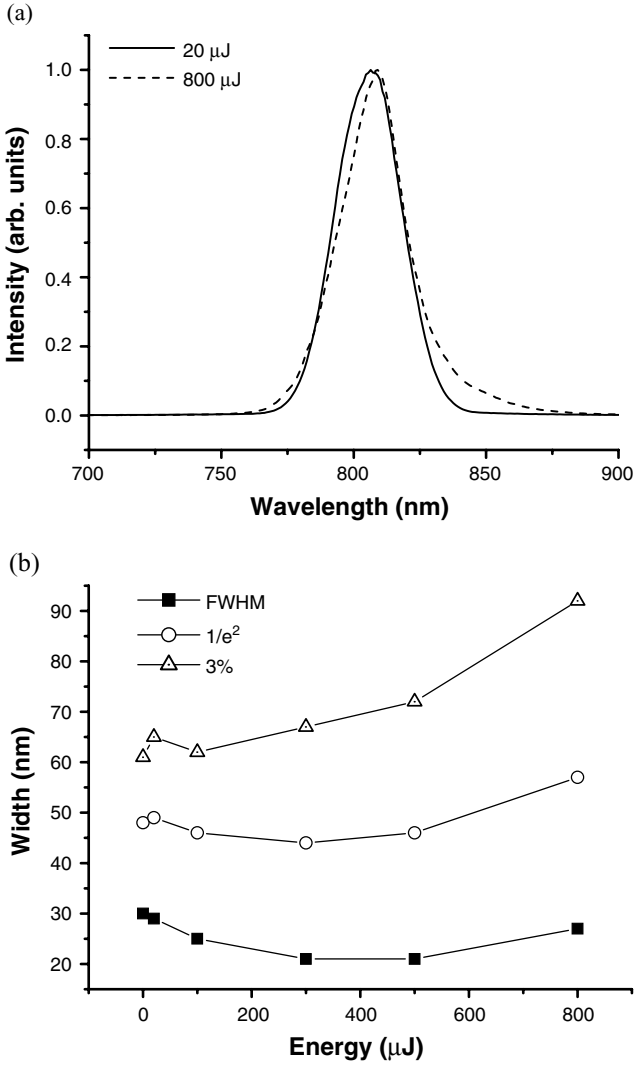

FIGURE 10 **a** Pulse spectra at 20 μJ (*solid line*) and 800 μJ (*dotted line*) obtained using the $f = 500$-mm lens. **b** Width of the spectrum as a function of the input energy at different levels (FWHM: *squares*, $1/e^2$: *circles*, 3%: *triangles*)

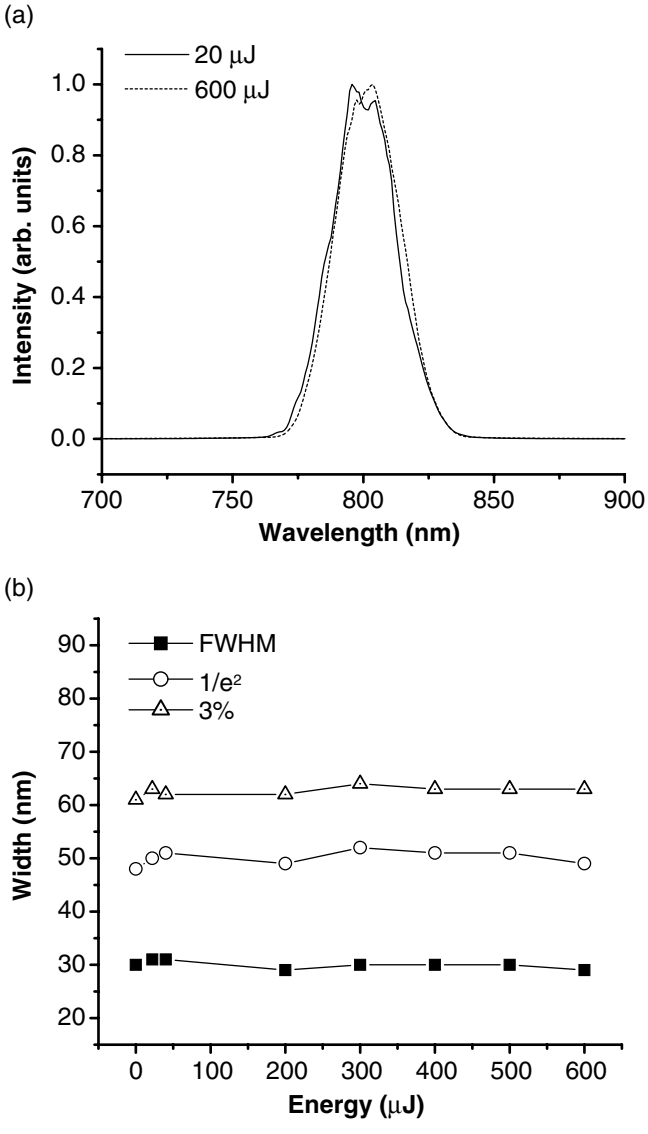

FIGURE 11 Same as Fig. 10, but for the $f = 200$-mm lens

weaker than those observed by Müller et al. One possible explanation for the large broadening in that experiment is that the spectrum was recorded after the exit window, which should obviously enhance the SPM. (We note that in our chamber white light can be generated in that window.) The role of active Raman modes of the neutral molecule and/or the parent ion, as proposed in [16], can be ruled out as the dominant effect for the enhancement of fragmentation in our observations. Because of its shorter duration, our pulse spectrum is wide enough to encompass the Raman transitions at all energies. But, the increase of the spectral density at the Raman frequencies is marginal for pulses with energies above 200 μJ, where the fragmentation rate increases enormously. The simple increase of the spectral density at the Raman frequencies due to the increase of the pulse energy is ruled out, since the increase in the fragmentation rate observed with the short focal length is much smaller than for the long focal length, while the spectral content is obviously the same.

5 Conclusions

In summary, the influence of the self-action effects, namely self-focusing and self-phase modulation, on the yields of ionization and fragmentation of toluene molecules interacting with an intense ultra-short Ti:sapphire laser pulse has been investigated using different focusing geometries. It has been shown that self-focusing of the pulse in the entrance window of the interaction chamber can lead to distortions of the spatial intensity distribution at the focus. First, whole-beam self-focusing leads to a displacement and misalignment of the focal area with respect to the detector opening. Second, small perturbations in the beam profile can be amplified to hot spots in the focal spot. Besides deviations from the Gaussian profile, the focal spot area increases with energy and the intensity does not scale linearly with energy and eventually saturates. It has been shown that these effects can be corrected by optimizing the position of the focusing lens and by a careful calibration of the energy-to-intensity dependence. Finally, a strong enhancement of the toluene fragmentation is related to linear (focusing geometry) and nonlinear (small-scale self-focusing) changes in the intensity distributions within the effective interaction zone. The Raman-mode excitation scenario is unlikely, which stresses the sensitivity of the fragmentation process to small changes in the intensity distribution.

ACKNOWLEDGEMENTS We acknowledge Francis Théberge for fruitful discussions. This work has been supported in Canada by the Canadian Research Chairs, the Canadian Foundation for Innovation (CFI), NSERC, DRDC-Valcartier, CIPI, Spectra Physics, and FQRNT. VPK and OGK acknowledge the support of the Russian Foundation for Basic Research, Grant No. 03-02-16939; VPK, OGK, and SLC acknowledge the support of the NATO Linkage Grant No. PST.CLG.976981. PA gratefully acknowledges support from the COPL during the fall–winter 2002–2003 and a Gay Lussac–Humboldt award. Support of the Alexander von Humboldt Foundation via a Research Award to SLC is highly appreciated.

REFERENCES

1 Y.R. Shen, *The Principles of Nonlinear Optics* (Wiley, New York, 1984)
2 R.W. Boyd, *Nonlinear Optics* (Academic, Boston, 1992)
3 A. Braun, G. Korn, X. Liu, D. Du, J. Squier, G. Mourou, Opt. Lett. **20**, 73 (1995)
4 S.L. Chin, A. Brodeur, S. Petit, O.G. Kosareva, V.P. Kandidov, J. Nonlinear Opt. Phys. Mater. **8**, 121 (1999)
5 V.P. Kandidov, O.G. Kosareva, I.S. Golubtsov, W. Liu, A. Becker, N. Aközbek, C.M. Bowden, S.L. Chin, Appl. Phys. B: Lasers Opt. **77**, 149 (2003)
6 J.H. Marburger, Prog. Quantum Electron. **4**, 35 (1975)
7 B.R. Suydam, IEEE J. Quantum Electron. **QE-11**, 225 (1975)
8 A.E. Siegman, *Lasers* (University Science Books, Sausalito, CA, 1986)
9 R.R. Alfano (ed.), *The Supercontinuum Laser Source* (Springer, New York, 1989)
10 W.J. Jones, B.P. Stoicheff, Phys. Rev. Lett. **13**, 657 (1964)
11 P.B. Corkum, C. Rolland, T. Srinivasan-Rao, Phys. Rev. Lett. **57**, 2268 (1986)
12 A. Brodeur, S.L. Chin, Phys. Rev. Lett. **80**, 4406 (1998)
13 A.L. Gaeta, Phys. Rev. Lett. **84**, 3582 (2000)
14 N. Aközbek, M. Scalora, C.M. Bowden, S.L. Chin, Opt. Commun. **191**, 353 (2001)
15 A.M. Müller, C.J.G.J. Uiterwaal, B. Witzel, J. Wanner, K.L. Kompa, J. Chem. Phys. **112**, 9289 (2000)
16 A.M. Müller, B. Witzel, C.J.G.J. Uiterwaal, J. Wanner, K.L. Kompa, Phys. Rev. Lett. **88**, 023001 (2002)
17 N.B. Delone, V.P. Krainov, *Atoms in Strong Light Fields* (Springer, Berlin, 1985)
18 S.A. Akhmanov, V.A. Vyslouh, A.S. Chirkin, *Optics of Femtosecond Laser Pulses* (American Institute of Physics, New York, 1992)
19 M. Decker, *Handbook of Nonlinear Optics* (Marcel Dekker, New York, 2003)
20 J. Muth-Böhm, A. Becker, F.H.M. Faisal, Phys. Rev. Lett. **85**, 2280 (2000)
21 J. Muth-Böhm, A. Becker, S.L. Chin, F.H.M. Faisal, Chem. Phys. Lett. **337**, 313 (2001)
22 M.W. Schmidt et al., J. Comput. Chem. **14**, 1347 (1993)
23 A. Becker, L. Plaja, P. Moreno, M. Nurhuda, F.H.M. Faisal, Phys. Rev. A **64**, 023408 (2001)
24 V.I. Bespalov, V.I. Talanov, Zh. Eksp. Teor. Fiz. Pis'ma Red. **3**, 307 (1966)